THE ASTROPHYSICAL JOURNAL, 421:570–580, 1994 February 1

HIGH-RESOLUTION IMAGES OF SHOCKED MOLECULAR CLUMPS IN THE SUPERNOVA REMNANT IC 443

JAN A. TAUBER,[1,2] RONALD L. SNELL,[3] ROBERT L. DICKMAN,[3,4] AND L. M. ZIURYS[5]
Received 1992 July 30; accepted 1993 August 6

ABSTRACT

We present high angular resolution interferometric observations of HCO^+ $J = 1 \rightarrow 0$ line emission from two molecular clumps which are being shocked by the blast wave from the supernova which formed the remnant IC 443. Our observations show that a range of gas densities exist within these clumps; this fact may explain the mixture of shock velocities inferred from other observations. Previous studies have shown evidence that molecular material is being accelerated by the blast wave in a systematic fashion around one of the clumps that we study. We show that this phenomenon also occurs at the small spatial scales that we observe. In addition, we present evidence that suggests that the velocity field may correspond to ablation from or a bow shock around the denser cores present within the clumps.

Subject headings: ISM: individual (IC 443) — ISM: molecules — molecular processes — shock waves — supernova remnants

1. INTRODUCTION

Supernova explosions may play and important role in star formation, and perhaps even in galaxy formation. However, the effect that these events have on their surrounding medium is still open to debate. Do supernova blast waves inhibit star formation, by dispersing the gas in their vicinity, or do they compress the gas, thereby propitiating the birth of new stars? The answer to these questions lies in the small-scale processes that take place during the interaction of the blast wave with the interstellar medium. Thus, the shocks associated with this interaction merit intensive and detailed study.

However, the interaction of supernova shock waves with their surrounding medium involves hydrodynamic processes which are not simple to analyze from a theoretical point of view. In addition, the spherical symmetry initially inherent in a supernova blast wave may be quickly lost as it is channeled by the dense and inhomogeneously distributed surrounding gas. An indication of the complexity of the phenomena involved is given by recent studies of the supernova remnant IC 443 (Wang & Scoville 1992; Turner & Lubowich 1991), which have shown that several different types of shock may coexist even within a small section of the shock front. Clearly, the real situation is much more complex than the simple models which have been developed to study it.

Among the known supernova remnants (SNRs), IC 443 is one of the few which shows clear-cut interaction between the shock and quiescent molecular gas. The cool gas associated with this object has been extensively surveyed in various molecular lines (De Noyer 1979a, b; Dickinson et al. 1980; De Noyer & Frerking 1981; Huang, Dickman, & Snell 1986; White et al. 1987; Ziurys, Snell, & Dickman 1989; Turner & Lubowich 1991; Wang & Scoville 1991; Dickman et al. 1992, hereafter DSZH), and atomic lines of hydrogen and oxygen (Braun & Strom 1986a, b; Burton et al. 1990). *IRAS* observations in the far-infrared have also been used to derive the properties of the dust in the region (Braun & Strom 1986a; Mufson et al. 1986). A careful study of the morphology of the region by Braun & Strom (1986a) reveals the existence of several non-concentric shells of accelerated molecular gas of which only one (named subshell A by the authors) is associated with accelerated molecular gas (DSZH). There is some controversy over the origin of this multishell morphology. Braun & Strom (1986a, b) believe that the shells are the shocked remains of bubbles blown by winds from young stars. An alternative model (e.g., Mufson et al. 1986) is that a single supernova blast wave expanding into a nonuniform medium is sufficient to account for the observed structure. In the rest of this study, we shall assume that the regions that we observe have been subject to the impact of a single blast wave from a supernova; this scenario is the most consistent with our observations.

It has recently become possible to image the shocked molecular hydrogen directly via emission from its vibrationally excited states. Maps of the H_2 1–0 $S(1)$ line (Burton et al. 1988, 1990) show a belt of shock-excited emission which outlines the region of interaction of the shell and the molecular cloud. Detailed models were developed by Burton et al. (1988, 1990) in an attempt to determine the type of shock operating in the region. The authors conclude that no single shock can explain all the available observations, and that a superposition of C-type shocks of varying velocities may be required. However, in this case the same ratio of area filling factors of slow and fast shocks should exist across the source, and this seems rather unlikely. The alternative to this model is a slow, partially dissociative J-type shock, which is thought to be unphysical (Burton et al. 1990). Clearly, large uncertainties still surround the details of the physical process occurring in this region, and more observations are required to understand them better.

In this work, we present high angular resolution interferometric images of line emission from the high-density molecular component. Our primary objective is to obtain a detailed view of the effects of the shock wave on the ambient molecular cloud at small spatial scales. The molecular cloud which interacts with the SNR has been surveyed at moderate angular resolution ($\sim 50''$) by Huang et al. (1986) and DSZH, using

[1] Radio Astronomy Laboratory, University of California, Berkeley, CA 94720.
[2] Current address: ESA Astrophysics Division, ESTEC, P.O. Box 299, NL-2200 AG Noordwijk, The Netherlands.
[3] Five College Radio Astronomy Observatory and Department of Physics and Astronomy, University of Massachusetts, Amherst, MA 01001.
[4] Current address: National Science Foundation, Washington, DC 20550.
[5] Departments of Chemistry and Astronomy, Arizona State University, Temple, AZ 85287.

observations of ^{12}CO $J = 1 \rightarrow 0$, ^{12}CO $J = 2 \rightarrow 1$, and HCO^+ $J = 1 \rightarrow 0$. Their maps have revealed the existence of highly perturbed molecular gas (identifiable by very large line widths) concentrated in clumps which lie along the periphery of an elliptical ring defined by more diffuse gas (in the remainder of this paper, we shall refer to the diffuse gas ring that links the clumps as the "ambient" gas). The kinematic structure of the clump suggests that the ring is expanding. The morphology of the H I emission (Braun & Strom 1986), and that of the belt of H_2 1–0 $S(1)$ and 60 μm emission observed in the region (Burton et al. 1990), resemble closely that of the ring of HCO^+. In addition to the wide line molecular emission, several narrow velocity features at velocities between -5 and 5 km s^{-1} have been observed by DSZH, mostly in the CO lines. These features probably correspond to quiescent (unshocked) gas in the local molecular cloud. The presence of many components in the molecular emission from the region leads to the overall picture outlined by DSZH, in which the blast wave from the supernova inpacts a thin, edge-on sheet of molecular material, illuminates its inner edge, and accelerates part of the gas in the molecular cloud radially outward from the source of the blast.

The most prominent of the perturbed molecular clumps have been observed by DSZH, but they are barely resolved even with their highest resolution (^{12}CO $J = 2 \rightarrow 1$) 23″ beam. The large masses that these authors estimate for the clumps suggest that they predate the time of the supernova explosion. The clumps thus represent originally quiescent gas which has been, or is being processed by the blast wave. We have obtained interferometric images at 5″ resolution of two of the clumps, in an attempt to study their structure in detail and to characterize the physical conditions created by the shock from the supernova blast wave. Out of the nine clumps of perturbed molcular material, the two that we have observed (labeled B and G by Huang et al. 1986) are the brightest in both CO and HCO^+ emission. Additionally, clump B possesses a strongly systematic internal velocity field (DSZH), which hints at the presence of material ablated from the clump surface by the shock wave. To situate B and G within the expanding ring of shocked material, we note that B appears to be located within the portion coming toward us, whereas G is close to its western rim, and thus may be moving transversely to us (also see Fig. 1).

For our observations we have used the $J = 1 \rightarrow 0$ line of HCO^+ as a probe, because its large dipole moment makes it sensitive to high gas densities ($> 10^5$ cm^{-3}), and because its spatial morphology is similar to that of other tracers of shocked gas in IC 443. Thus, we expect our observations to delineate the denser portions of the shocked ambient molecular cloud. In addition, HCO^+ is of interest because it figures highly in models of shock chemistry (Iglesias & Silk 1978; Elitzur 1983; Mitchell & Deveau 1983).

There has been some controversy in the past years about the measured abundance of HCO^+ in IC 443. The initial observations seemed to indicate a large enhancement (of up to a factor of 1000) of this species in the shocked regions (Dickinson et al. 1980; De Noyer & Frerking 1981; White et al. 1987). However, more recent observations (Ziurys et al. 1989; hereafter ZSD) of several transitions of HCO^+ and a more reliable multiline analysis indicate that the enhancement is at most of a factor of a few. This still poses problems in view of the fact mentioned above that the abundance of this species is expected to *decrease* in shocked regions. A recent multiline study of H_2CO emission (Turner & Lubowich 1991) in one of the clumps that we have observed (G), concludes that the H_2CO emission arises from very warm (> 300 K) and very dense ($> 10^6$ cm^{-3}) gas, but also that the gas must be very clumpy to explain single-dish HCO^+ observations. It is clear that it is necessary to have an adequate knowledge of the filling factor of each density phase before any conclusions on the abundances of several species can be drawn from the observations. In particular, Turner & Lubowich (1991) claim that previously measured values of the abundance of HCO^+ are unreliable because they do not take into account the fact that different transitions may arise from different gas phases and may thus fill the observed volume in different ways. The very high angular resolution ($\sim 5''$) obtained in this work improves considerably our knowledge of the filling factor of the HCO^+-emitting gas.

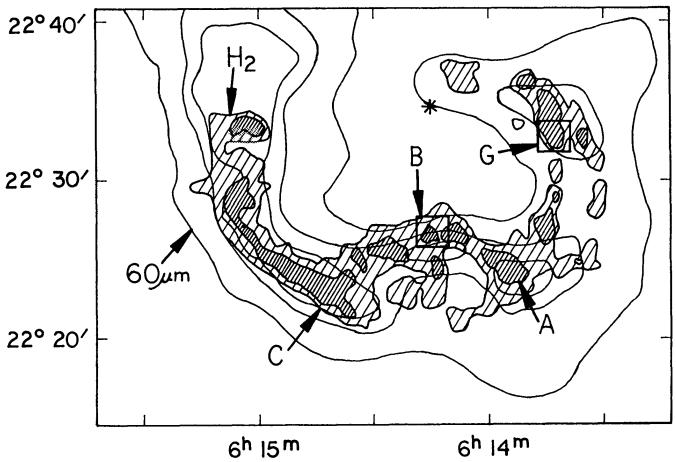

FIG. 1.—Overlay of maps of IC 443 in the emission of the *IRAS* 60 μm band (*contours*, from Braun & Strom 1986), and the emission of the H_2 1–0 $S(1)$ line from Burton (1988) (*hatched area*: heavier hatching emphasizes the H_2 emission peaks). The fields (B and G) that we have observed with the Hat Creek interferometer are outlined by the squares. Clumps A and C (DSZH) are also marked on this plot. A filled star (★) shows the location of the geometrical center of the supernova subshell (labeled "A" by Braun & Strom 1986a) that appears to be impacting on the molecular cloud.

2. OBSERVATIONS

We have observed two clumps of molecular material which show signs of shock excitation (as evidenced by extraordinarily broad molecular emission lines) with the BIMA three-element millimeter interferometer[6] in the $J = 1 \rightarrow 0$ emission line of HCO^+ at 89.18852 GHz. The two fields observed correspond to clumps B and G in the nomenclature of De Noyer (1979) and Huang et al. (1986). In Figure 1 we show the locations of these clumps relative to large-scale maps of the H_2 1–0 $S(1)$ and 60 μm emission. The observations were carried out between 1990 January and 1991 February, and include baselines from the compact, intermediate, and extended configurations of the array. The baselines range between 7.5 and 230 m in length, and provide a very well-sampled UV plane. The UV coverage implies that the array is not very sensitive to structures with angular dimensions greater than $\sim 40''$. During the observations, the data were amplitude and phase calibrated by observing the quasars 3C 273 and OJ 287 approximately every 30 minutes, and the planets whenever possible. The system

[6] The Berkeley Illinois Maryland Array is located at the Hat Creek Radio Observatory in California and is being developed and operated with partial funding from the National Science Foundation, under Grant AST 91-00307.

temperature was determined frequently using the chopper-wheel method of Penzias & Burrus (1973). The total sensitivity of the system at 89 GHz was determined to vary between ~ 200 Jy K^{-1} and ~ 800 Jy K^{-1}, although we only used data for which the wide-band phase calibrators indicated sensitivities of better than ~ 600 Jy K^{-1}. For the line observations, the correlators were set in such a way as to obtain 40 MHz of bandwidth divided into 128 channels, thus affording a velocity resolution of ~ 1.05 km s^{-1} per channel and a total velocity range of ~ 135 km s^{-1}. The line width at half-maximum was observed to be at most ~ 50 km s^{-1} in clumps B and G, so that they fit comfortably within the available bandwidth. The wide-band observations (used for quasar and planet calibrations) were made over a range of 320 MHz.

The data were reduced using the MIRIAD data reduction package developed at BIMA (Wright & Sault 1993). The calibrated visibilities were inverted using natural weighting to obtain the best signal-to-noise ratio, and simultaneous inverse weighting with respect to the system temperature. The beam synthesized with this scheme is symmetric and smooth above the 30% level, and exhibits no significant sidelobes within the 2′ field of view of the telescopes (see Fig. 2). The FWHM of a Gaussian fit to this beam is close to 5″ in both coordinates. The final images were produced using the CLEAN algorithm on 64×64 grids of 1″ pixel^{-1} for clump B and 1.″5 pixel^{-1} in the case of clump G, and binned in channels of 5 and 2 km s^{-1} width, respectively. These parameters were chosen so as to yield a similar peak signal-to-noise ratio in each of the two fields, and thus facilitate their comparison. The images were restored using 5″ FWHM Gaussian beams and are presented in Figures 3 and 4. The rms noise obtained in emissionless channels for each field is within 10% of the theoretically expected value. Clump G is somewhat more elongated than clump B, and its center is offset from the center of the observed field by ~ 20″ in Decl. and ~ 10″ in R.A. This does not pose large problems in terms of main beam attenuation, since most of the emission is still well within the FWHM of the beam of a single element of the array. However, we note that the maps that we present have not been corrected for the response of the inteferometer primary beam (110″). In particular, in field G the emission at the northern edge of Figure 4 may be as much as a factor of 2 brighter than is shown. In order to relate our results to single-dish observations, we have calculated the total flux that would be seen from these sources with a telescope such as the FCRAO 14 m antenna (~ 58″ FWHM), and compared to the single point observations of ZSD. In both cases the total flux seen by ZSD and that seen at Hat Creek are equal within reasonable absolute calibration errors (20%); thus the array has detected the vast majority of the HCO$^+$ emission originating within the primary beam of the interferometer (~ 110″ FWHM).

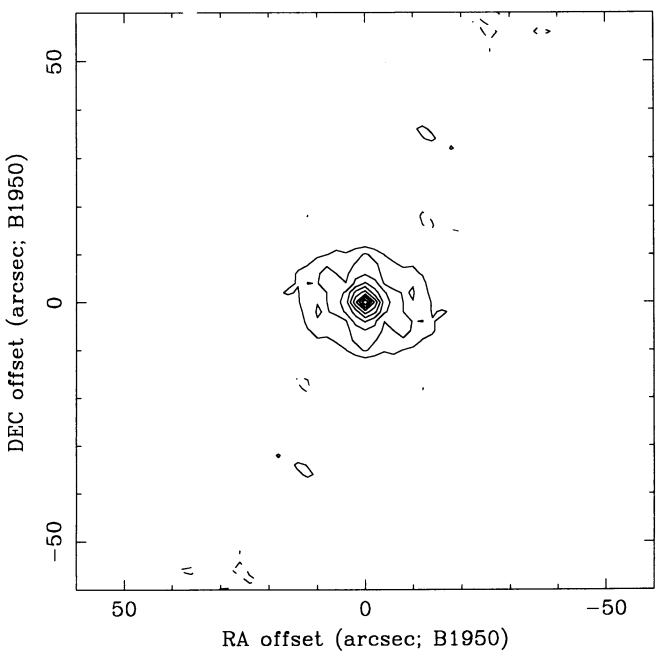

FIG. 2.—A plot of the synthesized beam resulting from natural weighting of the observed visibilities. The contours are in steps of 10% (negative contours are dashed lines). The beam lacks any significant sidelobes and is circularly symmetric above the 30% level. It is well fitted by a circular Gaussian with FWHM 5″.

In Figures 5 and 6 we present maps of different moments of the observed lines in clumps B and G. Figures 5*a* and 6*a* show the line intensity averaged over the whole velocity extent of the lines, obtained by averaging the channel maps in Figures 3 and 4, where the average includes only those channels whose intensity is above a given threshold. The thresholds that we have used correspond approximately to the rms noise in the channel maps, as determined from emissionless channels (~ 0.75 and 1.2 K for B and G, respectively). The technique of thresholding enhances the visibility of narrow velocity features relative to wider ones and is useful for locating clumps. Figures 5*b* and 5*d* and 6*b* and 6*d* were obtained after fitting Gaussian profiles at each pixel in Figures 3 and 4, and correspond to the fitted peak intensity, velocity centroid and FWHM velocity width. In the case of clump G, 3 channels (at -6, -4, and -2 km s^{-1}) were omitted from the fit since they are distorted by absorption from the ambient cloud, which has a mean velocity of -4 km s^{-1}.

3. SPATIAL AND KINEMATIC STRUCTURE

As is apparent from Figures 3–6, both clumps B and G have a similar appearance, consisting of several condensations aligned in a NE-SW orientation, and embedded in a more diffuse envelope of emission. Both fields appear to be clumpy: B can be roughly subdivided into four subclumps, and G into two. The characteristics of each subclump are shown in Tables 1 and 2, and typical spectra at the center of each of them are shown in Figures 7 and 8. The column densities of HCO$^+$ shown in the tables were calculated assuming that the lines are optically thin and in LTE, and that the LTE temperature is 50 K; although the former assumption is acceptable, the latter may not be (see ZSD). In order to calculate the clump masses shown in the tables we have estimated the abundance of HCO$^+$ in each clump by comparing the (high velocity) CO column density of DSZH to the HCO$^+$ column density calculated here; both are optically thin and trace the shocked gas (DSZH; ZSD).

The velocity field of clump B is much more clearly defined than that in clump G. Careful observation of the panels in Figure 5 indicates that regions of enhanced HCO$^+$ emission have narrower lines centered at velocities closer to that of the ambient molecular cloud (roughly -4 km s^{-1}). The reverse is also true: regions with low HCO$^+$ intensity emit lines which are wider (more perturbed) and are centered at more negative velocities. The spatial correlation of the peak HCO$^+$ line inten-

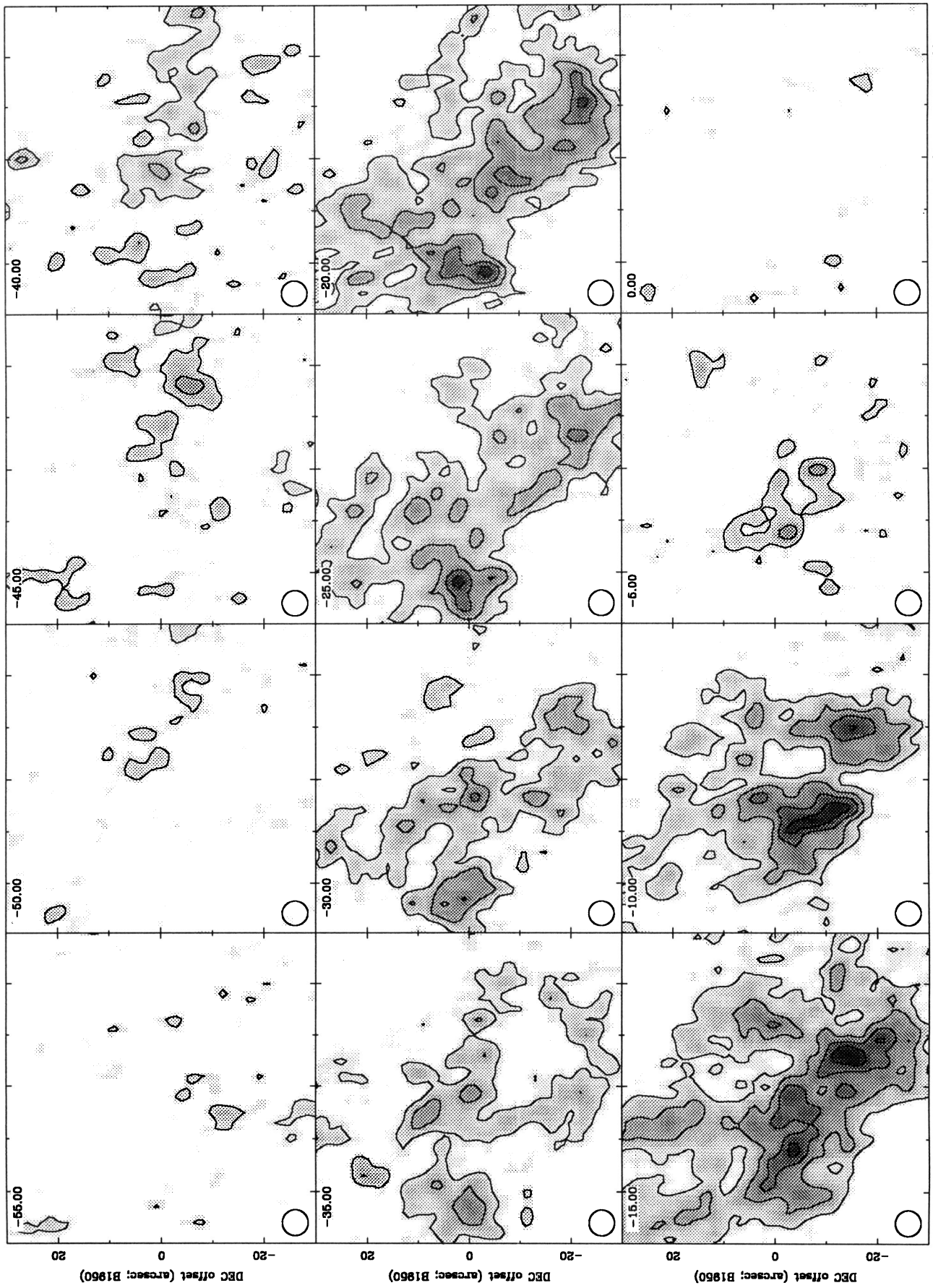

FIG. 3.—CLEANed channel maps of the HCO^+ emission from clump B. The central velocities of each channel are as marked; the width of each channel is 5 km s^{-1}. The pixel size is 2″, and the FWHM of the Gaussian restoring beam is 5″ (outlined in the lower left corner of each panel). The contours are in steps of 1.8 K (which corresponds to 20% of the peak value, 9 K). The linear gray scale ranges between 0.11 and 11 K. To convert K to Jy $beam^{-1}$ multiply the map values by 0.16. The spatial coordinates are in arcseconds offset from the center of the map, which is located at R.A. $06^h14^m15^s$, and Decl. 22°26′50″(1950).

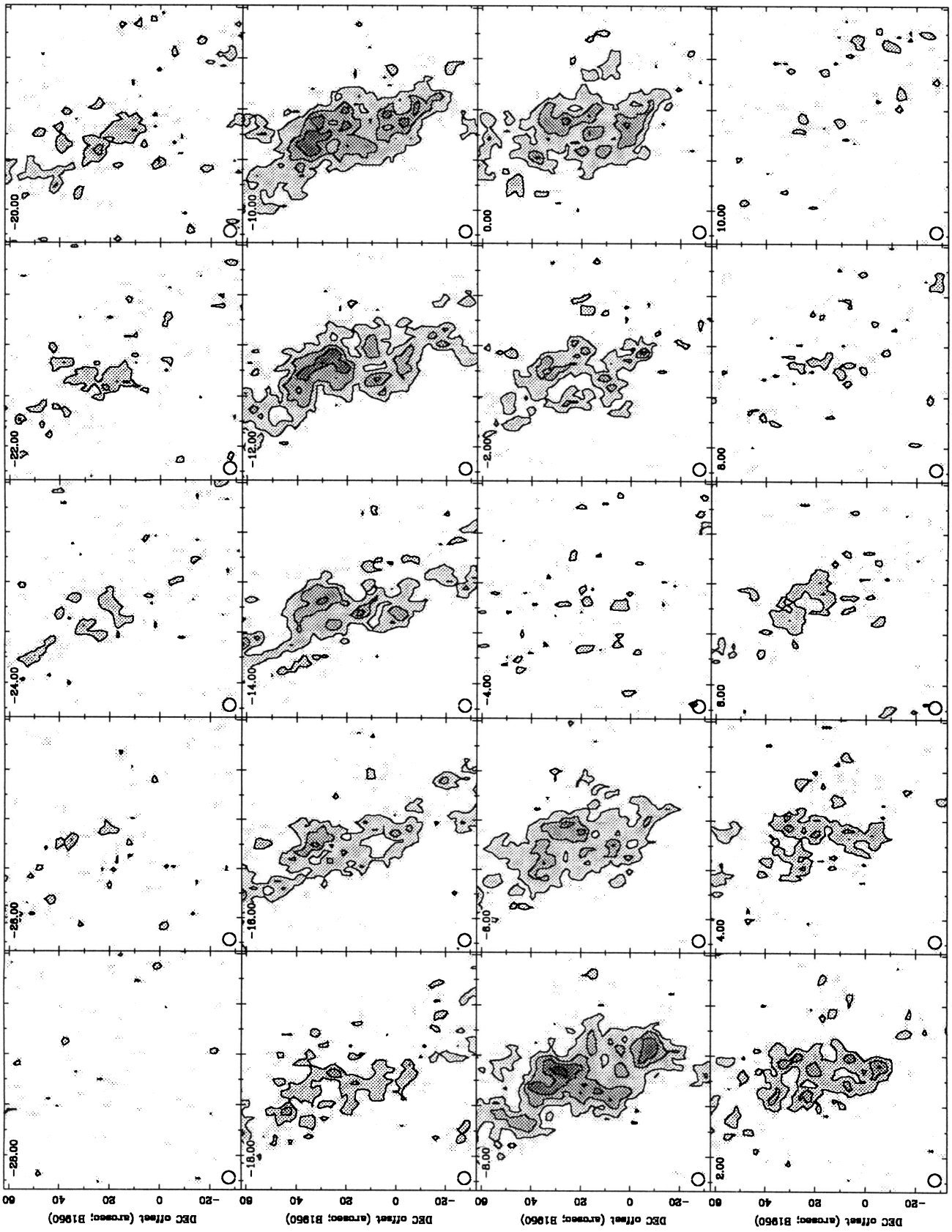

FIG. 4.—CLEANed channel maps of the HCO^+ emission from clump G. The central velocities of each channel are as marked; the width of each channel is 2 km s^{-1}. The pixel size is 1″.5, and the FWHM of the Gaussian restoring beam is 5″. The contours are in steps of 2.72 K (which corresponds to 20% of the peak value, 13.6 K). The linear gray scale ranges between 0.16 and 16 K. To convert K to Jy $beam^{-1}$ multiply the map values by 0.16. The spatial coordinates are in arcseconds offset from the center of the map, which is located at R.A. $06^h13^m40^s.4$, and Decl. 22°32′50″(1950). Foreground absorption from the ambient molecular cloud is clearly visible at velocities near −4 km s^{-1}.

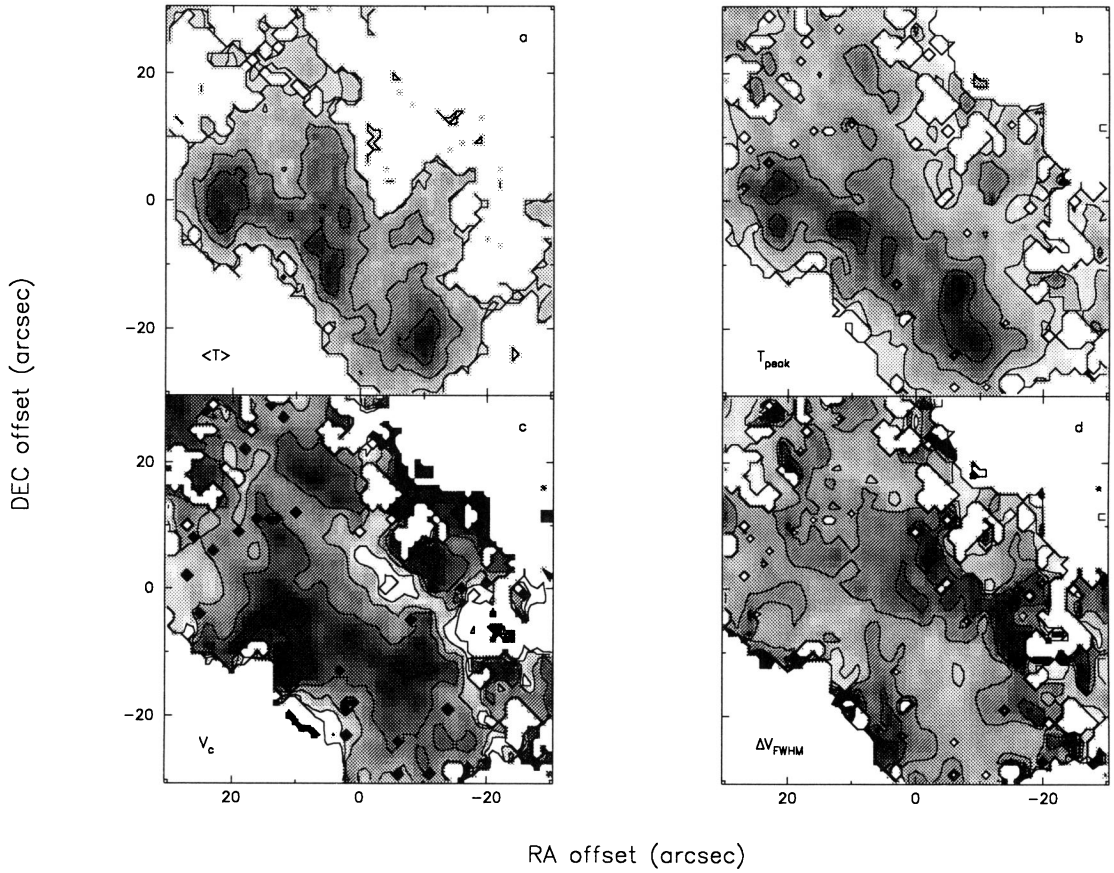

FIG. 5.—Maps of the moments of the HCO^+ emission from clump B. In panel (*a*) we show an average of the channel maps shown in Fig. 3, thresholded at a level equal to 1.5 times the rms noise in emissionless channels (~0.75 K). The contours are in arbitrary units, and are in steps of 20% of the peak value; the linear gray scale ranges between 12% and 120% of the peak value. The four subclumps which are analyzed in the text are clearly visible here (as well as in Fig. 3). Panels (*b*)–(*d*) were obtained after fitting a single Gaussian velocity profile to each pixel in Fig. 3. The panels correspond to peak line intensity (*b*), line center velocity (*c*), and FWHM line width (*d*). The contours are in steps of 1.54 K, 5 km s^{-1} (between −35 and −15 km s^{-1}), and 10 km s^{-1}, respectively; the linear gray scales vary between 0.93 and 9.3 K, −30 and −10 km s^{-1}, and 6 and 60 km s^{-1}, respectively. Panels (*b*)–(*d*) have been masked in such a way as not to show pixels for which the intensity of panel (*a*) of this figure is lower than 20% of the peak value; this limits the maps to that region where reliable Gaussian fits were obtained. A few bad fits are still apparent in panels (*c*) and (*d*) as very dark pixels. The spatial coordinates are in arcsecond offsets from the center of the maps (Fig. 3).

sity with both velocity width and centroid is clearly visible in Figure 5. We illustrate more quantitatively the correlation among the relevant variables in Figure 9; the fits shown are statistically significant (see figure caption). Apparently, the dense cores are moving toward us at a lower velocity than the lower density material which we see surrounding them. The unshocked gas in the local molecular cloud is situated at a velocity of −3 km s^{-1} toward clump B, and at −4 km s^{-1} toward clump G (DSZH). We note in Figure 9 that clump B shows a lack of emission at center velocities more positive than about −12 km s^{-1}. Thus, if the gas in clump B originally comoved with the quiescent molecular cloud, by now even the dense cores within it have been significantly accelerated toward us. Figure 7 indicates that the central portions of the subclumps are traveling toward us at velocites that vary between −15 and −25 km s^{-1}. Thus, if the dense cores originally had a

TABLE 1

CHARACTERISTICS OF SUBCLUMPS IN CLUMP B

SUBCLUMP	EXTENTS[a] ΔR.A.	EXTENTS[a] ΔDecl.	T_{peak}(ave)[b] (K)	T_{peak}(max)[b] (K)	v_c(ave) (km s^{-1})	ΔV_{FWHM}(ave) (km s^{-1})	N(ave)[c] ($\times 10^{14}$ cm^{-2})	N(max)[c] ($\times 10^{14}$ cm^{-2})	MASS[d] ($M_\odot$)
B1.....	14″ → 30″	−15″ → 12″	3.5	6.5	−24	24	2.3	4.9	0.9
B2.....	−2 → 14	−30 → 15	3.8	7.7	−20	28	2.5	5.0	1.7
B3.....	−20 → −2	−30 → −9	4.2	8.5	−20	22	2.9	5.2	1.0
B4.....	−25 → −2	−9 → 10	2.7	6.2	−22	30	2.2	3.8	0.8

[a] In arcsecond offsets from the center of the map (see Fig. 3).
[b] The peak line temperature derived from a Gaussian fit to the observed profiles.
[c] HCO^+ column density (cm^{-2}), obtained using a kinetic temperature of 50 K.
[d] Molecular (H_2) mass (in $M_\odot$), obtained using a distance to the source of 1500 pc, and an abundance of HCO^+ of 10^{-7} relative to that of H_2. The latter was derived using a value for the abundance of CO of 10^{-4}, as in DSZH (see text). The total mass in the clumps is ~4.4 $M_\odot$.

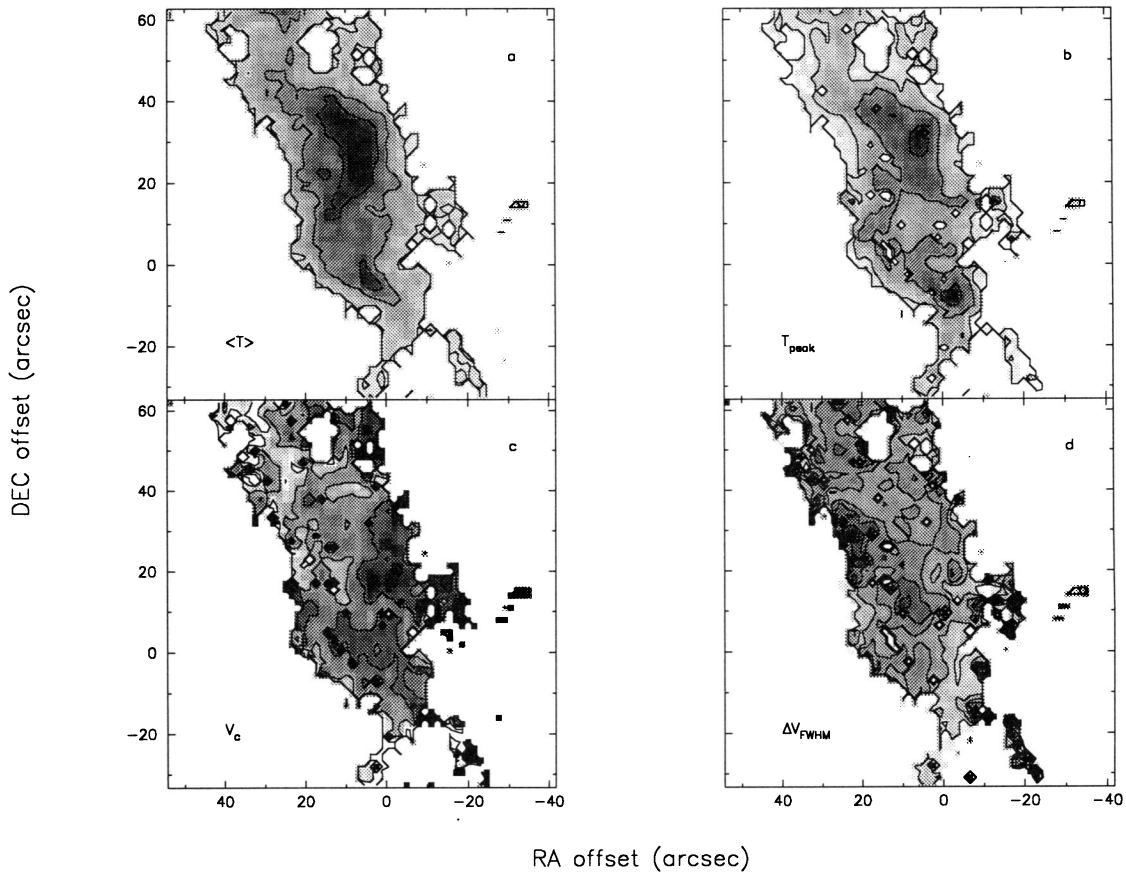

FIG. 6.—Maps of the moments of the HCO^+ emission from clump G. In panel (*a*) we show an average of the channel maps shown in Fig. 4, thresholded at a level equal to the rms noise in emissionless channels ($\sim$1.2 K). The contours are in arbitrary units, and are in steps of 20% of the peak value. The two subclumps which are analyzed in the text are clearly visible here (as well as in Fig. 3). Panels (*b*)–(*d*) were obtained after fitting a single Gaussian velocity profile to each pixel in Fig. 3. The panels correspond to peak line intensity (*b*), line center velocity (*c*), and FWHM line width (*d*). The contours are in steps of 2.46 K, 3 km s^{-1} (between −15 and −3 km s^{-1}), and 5 km s^{-1} (between 10 and 35 km s^{-1}), respectively; the linear gray scales range between 1.5 and 15 K, −12 and 0 km s^{-1}, and 5 and 50 km s^{-1}, respectively. Panels (*b*)–(*d*) have been masked in such a way as not to show pixels for which the intensity of panel (*a*) of this figure is lower than the 20% level (first contour); this limits the maps to that region where reliable Gaussian fits were obtained. A few bad fits are still apparent in panels (*c*) and (*d*) as very dark pixels. The spatial coordinates are in arcsecond offsets from the center of the maps (Fig. 4).

typical velocity of about −4 km s^{-1} then they have gained from the SN blast wave velocities which range between 12 and 20 km s^{-1}.

The case of clump G is less clear: the spatial correlation between the HCO^+ intensity and the velocity field is less marked (Fig. 6), as is the anticorrelation between the line center velocity and the line width (Fig. 9), although the latter is still present. In addition, there still is a significant amount of emission at and near the velocity of the quiescent molecular cloud (Fig. 9). Finally, as noted before, clump G appears to have much less internal structure than clump B. Its location in the "expanding ring" suggests that G is close to the western edge of the rim; thus, projection effects probably play a major role in the observed structure and velocity field of G, reducing the line-of-sight velocity components (DSZH).

4. DISCUSSION

The clear correlation of the velocity centroid and dispersion of the HCO^+ line emission with its spatial distribution (demonstrated in § 3), shows that the motion of the gas in the

TABLE 2

CHARACTERISTICS OF SUBCLUMPS IN CLUMP G

SUBCLUMPS	EXTENTS[a] ΔR.A.	EXTENTS[a] ΔDecl.	T_{peak}(ave)[b] (K)	T_{peak}(max)[b] (K)	v_c(ave) (km s^{-1})	ΔV_{FWHM}(ave) (km s^{-1})	N(ave)[c] ($\times 10^{14}$ cm^{-2})	N(max)[c] ($\times 10^{14}$ cm^{-2})	MASS[d] ($M_\odot$)
G1.....	−25 → 45	5 → 55	4.6	11.5	−8	20	2.6	6.3	10.6
G2.....	−20 → 30	−25 → 5	4.6	12.3	−8	16	1.3	5.5	2.1

[a] In arcsecond offsets from the center of the map (see Fig. 4).

[b] The peak line temperature derived from a Gaussian fit to the observed profiles (absorbed channels at −6, −4, and −2 km s^{-1} were not included in the fit).

[c] HCO^+ column density (cm^{-2}), obtained using a kinetic temperature of 50 K.

[d] Molecular (H_2) mass (in $M_\odot$), obtained using a distance to the source of 1500 pc, and an abundance of HCO^+ of 7.3×10^{-8} relative to that of H_2. The latter was derived using a value for the abundance of CO of 10^{-4}, as in DSZH (see text). The total mass in the clumps is 12.7 $M_\odot$.

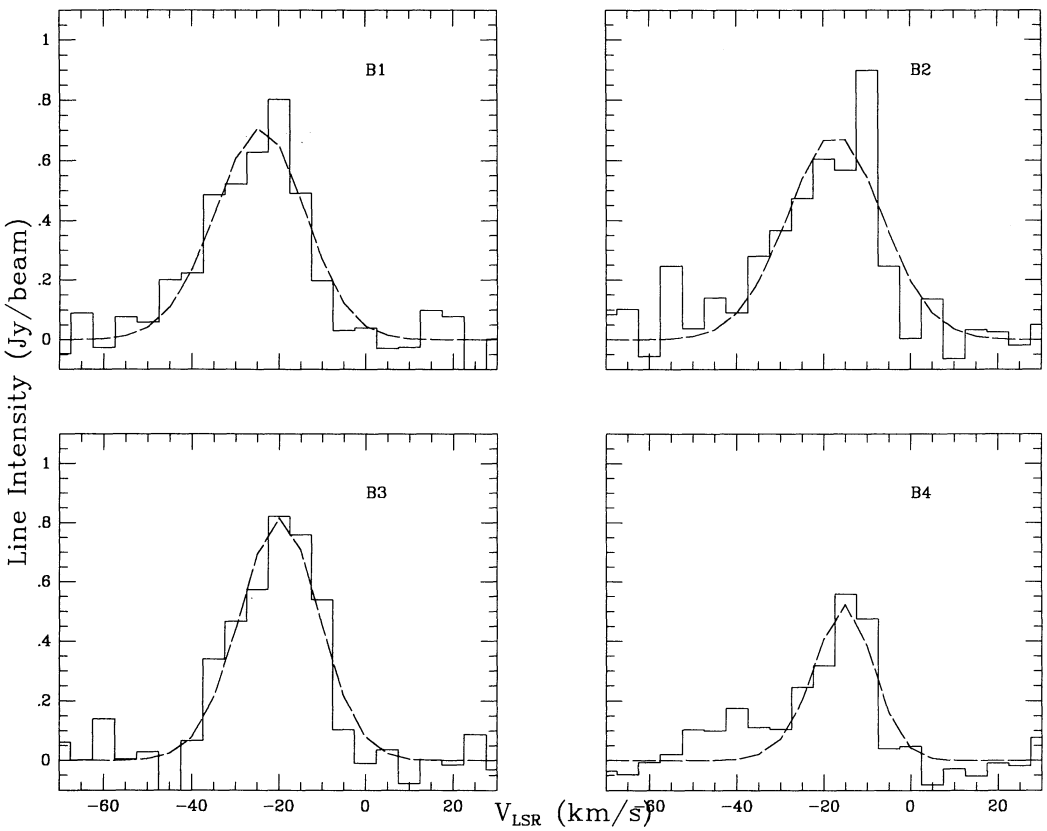

FIG. 7.—We show synthesized HCO^+ spectra (*solid lines*) at the central positions of each of the subclumps B1, B2, B3, and B4 identified in clump B. The dashed lines show the Gaussian fits. The rms noise in the spectra is ~ 0.12 Jy beam^{-1}. See Table 1 for the central positions and the spatial extent of each subclump.

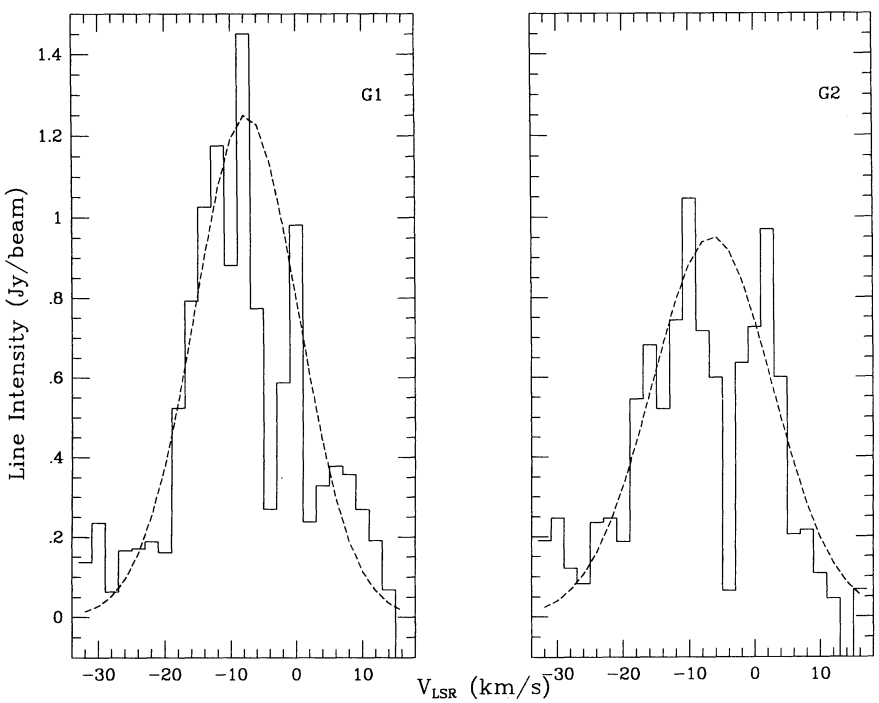

FIG. 8.—We show synthesized HCO^+ spectra (*solid lines*) at the central positions of each of the subclumps G1 and G2 identified within clump G. The dashed lines show the Gaussian fits. The rms noise in the spectra is ~ 0.2 Jy beam^{-1}. See Table 2 for the central positions and the spatial extent of each subclump.

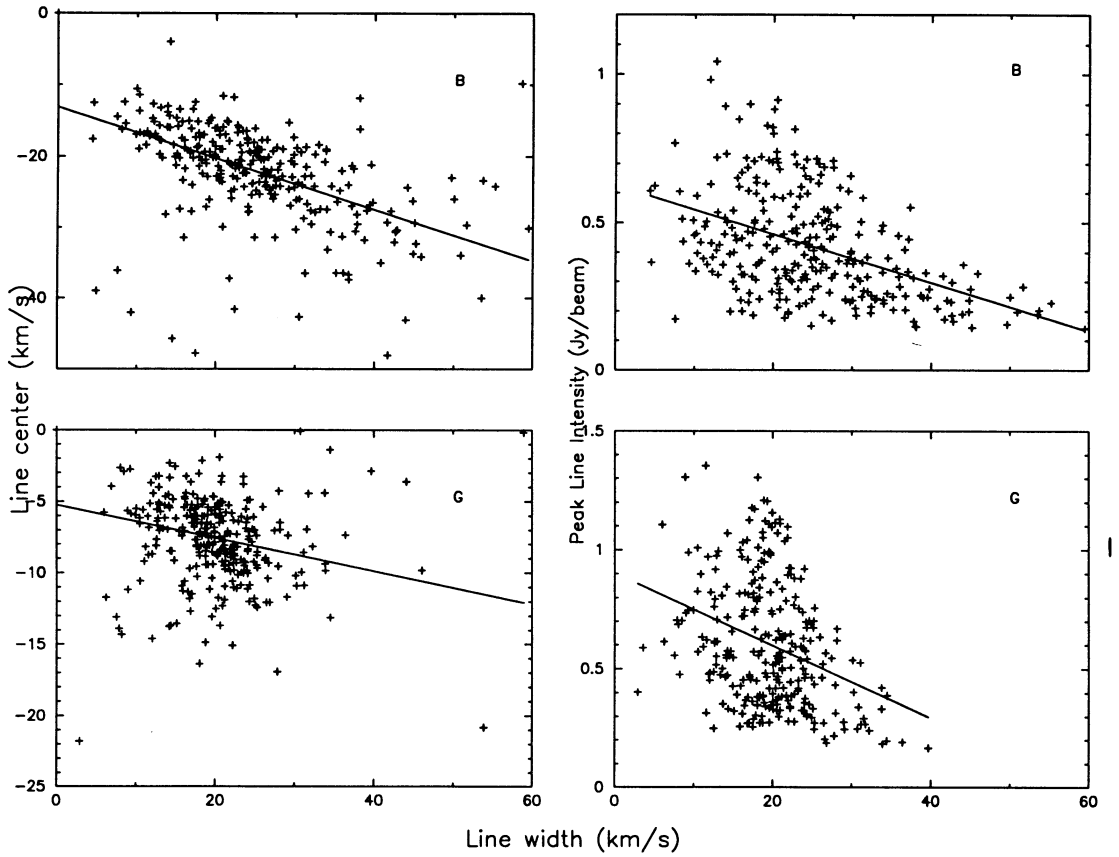

FIG. 9.—The four panels show the relationship between the line center velocity and line width (*left-hand side*) and between the peak line intensity and line width (*right-hand side*) in each of clumps B (*upper half*) and G (*lower half*). The plotted quantities were derived from Gaussian fits to each pixel in the synthesized maps. Since the beam size is larger than the pixel size, we have only plotted every third pixel for clump B and every second pixel for clump G to preserve pixel-to-pixel independence. The plots for clump B show a clear correlation, whereas in clump G, although a correlation is undoubtedly present, it is much less pronounced. The lines drawn in each panel represent a least-squares fit of the points to a linear function. To estimate the goodness of the fit, we use as a parameter χ^2 divided by the number of degrees of freedom. χ^2 is estimated using a constant error bar for the data points corresponding to one velocity bin for the velocity related parameters, and 15% for the peak line intensities. The goodness-of-fit parameter should be close to unity for a reasonable fit. The calculated values of this parameter are: 1.5 (B, line center); 1.5 (B, line intensity); 2.5 (G, line center); and 3.5 (G, line intensity). The fits for clump B are clearly "better" than those for clump G.

field observed is *not* purely random or turbulent. Additionally, in the case of B there is evidence that a systematic velocity field exists at larger spatial scales: at a distance of $\sim 3''.5$ on either side of the center of B, *atomic* gas has been accelerated to velocities as high as -90 km s^{-1} (Braun & Strom 1986a); at $\sim 2'$, we can already see *molecular* gas at a velocity of ~ -75 km s^{-1} (DSZH); finally, our own observations show spots of molecular emission with velocity ~ -60 km s^{-1} at a distance of $\sim 15''$ from individual cores (Fig. 9). This is quite contrary to expectations, since numerical simulations of blast waves impacting on dense spherical clumps (Klein, McKee, & Colella 1990; Stone & Norman 1992) show no signs of the development of systematic flows. Rather, the simulations indicate that the clumps are totally fragmented in a relatively short time, corresponding to a few cloud-crushing timescales. For a 100 km s^{-1} shock velocity and a 0.5 pc clump ($\sim 60''$), the crushing time is ~ 5000 years, while Petre et al. (1988) have estimated the age of the SNR to be ~ 3000 years. These numbers are of course very uncertain (probably by factors of a few), but the possibility remains that the blast wave has only interacted for a very short time with the clumps, and that they are still in the process of being destroyed. However, even before total destruction takes place, the simulations do not appear to show systematic velocity fields being formed.

However, the *observational* evidence for a systematic velocity field is persuasive. It may be that the blast wave from the SN is now encountering a clumpy foreground molecular cloud. In fact, DSZH had already suggested this scenario. In that case, the preexisting density perturbations within the cloud, although insufficiently large initially to produce detectable HCO^+ emission (see DSZH), are compressed, heated, and accelerated by the blast wave and are now capable of generating detectable emission. HCO^+ is now detectable either because it has been heated by the shock, and/or because its abundance has increased by chemical processes in the shocked layers. The latter has been shown to be possible for short periods of time after the passage of a strong shock (Mitchell & Deveau 1983).

What is the origin of the large line widths observed in the molecular emission from these clumps? It is probable that gas turbulence plays a major role in the kinematics of the clumps; in Figure 9*a*, the line centroids do not go much more negative than about 35 km s^{-1}, but there is emission at least until -60 km s^{-1}. The large line widths would also indicate that there is a significant amount of turbulence distributed throughout the clump and not just in the lower density envelope. However, turbulence alone can explain the line widths themselves but not the systematic shift of the velocity centroid as a function of

gas column density. Thus, we conclude that molecular gas has been accelerated by the blast wave in a systematic fashion towards us, and now is distributed in a large range of bulk velocities. The high-velocity molecular gas could originate in low-density (hence high shock velocity) preshock molecular material, or could have been dragged by the blast wave from the denser subclumps in a bow-shock type of velocity field. The shock velocity implied by the high-velocity emission seen in clump B both in H I and in HCO^+ is at least ~ 80 km s^{-1}. For strong shocks, the shock velocity decreases as the inverse square root of the preshock gas density, assuming a constant blast wave velocity and density of the surrounding medium (Klein, McKee, & Colella 1990). The column densities observed indicate that the gas density probably increases by at least an order of magnitude in each subclump from the location of the highest velocity gas to the center. Thus, the shock velocities near the core of each subclump could easily be as low as 20 km s^{-1}, and increase rapidly with distance from the core. Shock velocities less than ~ 50 km s^{-1} are not fast enough to dissociate molcules, but higher velocities will (Hollenbach & McKee 1980). It is clear then that the dissociation characteristics of the shock may vary drastically from the core to the envelope of the clump, and in particular the lower density regions of the clumps are probably subject to dissociative shocks.

If there are indeed bow-shock type velocity fields around the subclumps in B and G, then we should expect to see a typical signature in the velocity structure of the emission. In the simplest picture of a bow shock, gas will be dragged by the blast wave at constant velocity around the surface of a dense clump. The observable velocity structure will then be determined by the component of the velocity vector (tangent to the clump surface) along the line of sight to the observer. The arbitrariness of the viewing angle can produce a variety of signatures. Consider two specific orientations, which we argue might correspond roughly to clump B (the bow shock in the line of sight of the observer), and to clump G (the bow shock across the line of sight of the observer). These orientations are deduced from the positions of the clumps in the "expanding ring" of DSZH. In the first case, one would expect the most extreme emission velocities to occur symmetrically at the largest impact parameters. Qualitatively this is what is seen in Figure 10*a*, where there are two spots of high-velocity emission at roughly -60 km s^{-1} located symmetrically with respect to the nucleus of subclump B3. In the second case (G2), we expect the line dispersion to be widest where the blast impacts the subclump, and narrowest at the opposite side of the subclump, where the line-of-sight velocity components are small. There is a suggestion of this behavior in Figure 10*b*, at least for the lowest-level contours. This evidence is ambiguous at best, and observations

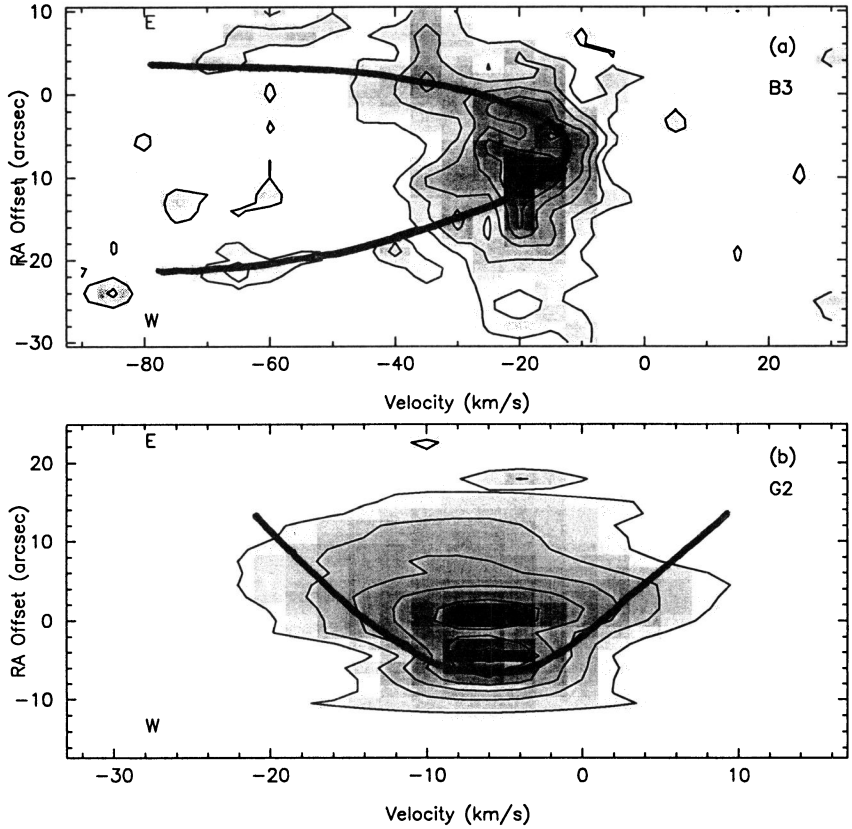

FIG. 10.—In this figure we show position-velocity diagrams along the R.A. axis of the HCO^+ $J = 1 \rightarrow 0$ emission for subclump B3 and G2. These diagrams were generated from the channel maps in Fig. 3 in the case of clump B; for clump G, we have used our Gaussian fit models (§ 2), because the absorbed channels visible in the data of Fig. 4 render the interpretation of position velocity maps difficult. The spatial offsets are measured in arcseconds from the pointing center for each clump (see Figs. 3 and 4). In each case, the constant coordinate offset is (*a*) B3: ΔDecl. $= -22''$, and (*b*) G2: ΔDecl. $= -5''$. The contours are in steps of 1.11 K, and 1.53 K for B3 and G2, respectively; the gray scale is linear and varies between 0.4 and 7.72 for B3, and between 0.4 and 10 K for G2. The heavy lines indicate qualitatively what the highest line-of-sight velocity components would be if gas were dragged by a blast wave around the periphery of a dense clump. In the upper panel the direction of impact is assumed to lie in the line of sight, whereas in the lower panel it is assumed to be perpendicular to the line of sight.

with much better signal-to-noise ratios are clearly needed to compare more incisively the model with the data.

Finally, we note that the range of gas densities present within the clumps probably results in a variation of the type and velocity of the blast-wave–induced shock across these regions, and this variation in turn provides a natural explanation for the multiple shock speeds that Burton et al. (1990) require to explain their O I observations. We note that Burton et al. (1990) conducted their observations at the position of clump C (see Fig. 1), which exhibits similar characteristics to clumps B and G.

5. SUMMARY AND CONCLUSIONS

The supernova which formed the remnant IC 443 gave rise to a blast wave which is still interacting with a nearby molecular cloud. The molecular emission from the interacting region consists mainly of a belt of diffuse emission arising from shocked gas, several well-localized clumps which give rise to emission lines whose intensity and width are larger than in the diffuse belt, and several narrow velocity features which represent quiescent (unshocked) cold gas. We have conducted high angular resolution observations of the $J = 1 \rightarrow 0$ line of HCO^+ toward two of the localized clumps.

At small spatial scales, we find dynamical evidence that a blast wave is indeed processing the two clumps. The spatial and kinematic morphology that we observe shows that the blast wave is accelerating molecular gas to high velocities. This fact is especially clear for clump B, and less so for clump G, probably because much of the bulk gas motion in G is transverse to the line of sight.

The spatial morphology of the emission indicates that a range of gas densities exist within the clumps. This fact provides a natural explanation for the existence of shocks at varying velocities, as inferred previously (Burton et al. 1990). Close to the dense cores which exist within each clump, the shock velocities are low and the molecules are not dissociated. The shock velocity increases outward and the shock becomes dissociating; at larger distances the molecular gas has been dissociated and only atomic gas subsists. Because the lower density gas may be subject to dissociating shocks, and because of the systematic velocity field observed in clump B at a variety of size scales, we suggest that the high-velocity molecular gas has been dragged by the blast wave from the denser gas within the clumps in an ablation or bow-shock type of flow field. Evidence of bow-shock signatures around the subclumps is ambiguous (Fig. 10), and observations with better signal-to-noise ratio are required to settle this question. The existence of bow shocks at small spatial scales within the clumps would go against the present wisdom that dense clumps subject to SN blast waves are quickly and completely destroyed, without ever developing systematic velocity fields.

Additional high angular resolution observations of other wide line clumps in the region may help us to understand better some of the issues raised in this work. The study of bow-shock type velocity fields in clumps situated around the periphery of the belt of shock-excited gas may allow us to pin down the exact location of the source of the blast wave, much as is done with jets and Herbig-Haro objects (Raga & Böhm 1986; Hartigan, Raymond, & Meaburn 1990). The temperature structure of the bow shocks needs to be determined; this can be done by choosing appropriate molecular tracers. Finally, we point out that the size of the SNR and the time scale for propagation of the blast wave imply that there may be significant time lags between the impact of the blast wave on clumps situated in different locations. Thus, the possibility exists that from among the wide line clumps we could extract a set which represent different evolutionary stages of shock processed molecular clumps. Such a situation would enable us to test whether clumps of gas are indeed completely destroyed and dispersed by the impact of a supernova blast wave, as is currently suggested by numerical simulations.

REFERENCES

Braun, R., & Strom, R. G. 1986a, A&A, 164, 193
———. 1986b, A&AS, 63, 345
Burton, M. G., Geballe, T. R., Brand, P. W. J. L., & Webster, A. S. 1988, MNRAS, 231, 617
Burton, M. G., Hollenbach, D. J., Haas, M. R., & Erickson, E. F. 1990, ApJ, 355, 197
De Noyer, L. K. 1979a, ApJ, 228, L41
———. 1979b, ApJ, 232, L165
De Noyer, L. K., & Frerking, M. A. 1981, ApJ, 246, L37
Dickinson, D. F., Rodriguez-Kuiper, E. N., Dinger, A. S., & Kuiper, T. B. H. 1980, ApJ, 237, L43
Dickman, R. L., Snell, R. L., Ziurys, L. M., & Huang, Y.-L. 1992, ApJ, 700, 203 (DSZH)
Elitzur, M. 1983, ApJ, 267, 174
Hartigan, P., Raymond, J., & Meaburn, J. 1900, ApJ, 362, 624
Hollenbach, D. J., & McKee, C. F. 1980, ApJ, 241, L47
Huang, Y.-L., Dickman, R. L., & Snell, R. L. 1986, ApJ, 302, L63
Iglesias, E., & Silk, J. 1978, ApJ, 226, 851
Klein, R. I., McKee, C. F., & Colella, P. 1990, in The Evolution of the Interstellar Medium, ASP Conf. Ser., Vol. 12, ed. L. Blitz (San Francisco: ASP), 117
Mitchell, G. F., & Deveau, T. J. 1983, ApJ, 266, 646
Mufson, S. L., McCollough, M. L., Dickel, J. R., Petre, R., White, R., and Chevalier, R. 1986, AJ, 92, 1349
Penzias, A. A., & Burrus, C. A. 1973, ARA&A, 11, 51
Petre, R., Szymkowiak, A., Seward, F. D., & Willingale, R. 1988, ApJ, 335, 215
Raga, A. C., & Böhm, K. H. 1986, ApJ, 308, 829
Stone, J. M., & Norman, M. L. 1992, ApJ, 390, L17
Tielens, A. G. G. M., & Hollenbach, D. J. 1985, ApJ, 291, 722
Turner, B. E., & Lubowich, D. A. 1991, ApJ, 381, 173
van Buren, D., & MacLow, M.-M. 1994, in preparation
Wang, Z., & Scoville, N. Z. 1992, ApJ, 386, 158
White, G. J., Rainey, R., Hayashi, S., & Kaifu, N. 1987, A&A, 173, 337
Wright, M. C. H., & Sault, R. J. 1993, ApJ, 402, 546
Ziurys, L. M., Snell, R. L., & Dickman, R. L. 1989, ApJ, 341, 857 (ZSD)